Ceramics International 51 (2025) 16061–16072

Contents lists available at ScienceDirect

Ceramics International

journal homepage: www.elsevier.com/locate/ceramint

Low temperature Al/AlN joint by Ag sinter paste from 180 °C: Interface formation and joint reliability

Chuantong Chen [a,*], Li Liu [b,**], Fupeng Huo [a], Dongjin Kim [c], Sangmin Lee [a], Wanli Li [d], Katsuaki Suganuma [a]

[a] Institute of Scientific and Industrial Research, SANKEN, Osaka University, Address, Japan
[b] School of Materials Science and Engineering, Wuhan University of Technology, Wuhan, 30070, China
[c] Korea Institute of Industrial Technology (KITECH), Yeonsu-gu, Incheon, 21999, Republic of Korea
[d] Jiangsu Key Lab of Advanced Food Manufacturing Equipment and Technology, Jiangnan University, Jiangsu, 214122, China

ARTICLE INFO

Handling Editor: Dr P. Vincenzini

Keywords:
Metal/ceramic direct bonding
Molecular dynamics simulation
Ag sinter paste
Microstructure evolution
High-temperature storage
Interface bonding

ABSTRACT

This study introduces a novel technology for direct bonding of bare aluminum (Al) to aluminum nitride (AlN) ceramics using Ag sinter paste under low-temperature conditions starting from 180 °C, and air environments. A robust interface shear strength of up to 40.5 MPa was achieved at a low sintering temperature of 300 °C under a pressure of 5 MPa, significantly lower than the melting point of Al (660 °C). Transmission Electron Microscopy (TEM) observations revealed that Ag particles attach to and inter-diffuse into the natural oxide layer of Al (Al_2O_3) and the AlN layers during the initial stages of sintering, forming a porous structure after sintering. Additionally, the interface bonding mechanism for Ag/Al and Ag/Al_2O_3 was analyzed using Molecular Dynamics (MD) simulations. The results indicated that the diffusion of Ag into Al_2O_3 occurs moderately faster than into Al, suggesting that the Al_2O_3 layer facilitates interface bonding for Ag during low-temperature, low-pressure sintering. The high-temperature reliability of the Al/AlN bonding structure was also examined by aging it at 300 °C for 500 h. Despite the microstructural evolution within the bonding layer, the shear strength remained above 20 MPa after aging, demonstrating excellent high-temperature stability.

1. Introduction

The integration of wide band-gap (WBG) semiconductors into power electronic systems allows these devices to operate at high switching speeds and elevated temperatures (above 250 °C), thanks to their superior voltage-blocking capabilities, high-temperature endurance, and fast switching frequencies. In WBG power modules, the die-attach materials, which bond WBG dies to ceramic-based substrates such as copper (Cu)-ceramic-Cu and aluminum (Al)-ceramic-Al, are critical for ensuring optimal performance in environments reaching 250 °C [1,2]. The Cu-ceramic-Cu structure, depending on the fabrication process, is commonly referred to as direct-bonded copper (DBC) or active metal brazing (AMB). Similarly, the Al-ceramic-Al configuration is recognized as a direct-bonded aluminum (DBA) substrate. Among ceramic substrates, aluminum nitride (AlN) stands out as a preferred material due to its desirable properties, including similar density, strength, and hardness to silicon carbide (SiC) and aluminum oxide (Al_2O_3), as well as significantly higher thermal conductivity. Moreover, the low coefficient of thermal expansion (CTE) of AlN closely matches that of SiC, making it an excellent candidate for electronic packaging applications [3,4]. Recent advancements highlight the growing implementation of DBA substrates utilizing AlN as alternatives to DBC substrates, particularly in insulated gate bipolar transistor (IGBT) modules for hybrid electric vehicles. Studies have demonstrated that DBA substrates exhibit exceptional performance under thermal cycling conditions, further validating their potential in high-reliability applications [5,6].

For effective Al/AlN ceramic bonding, enhancing the wetting properties and reducing the contact angle between Al and AlN ceramics are crucial for achieving reliable bonding performance. Traditionally, this requires annealing at temperatures above the melting point of Al (~660.3 °C) [7,8]. Recent studies have shown that alloying Al with 0.42 at% Mg and 0.38 at% Si can lower its melting point, enabling bonding with AlN at a reduced temperature of 650 °C under vacuum. Additionally, the use of a CuO interlayer has been reported, where the reduction

* Corresponding author.
** Corresponding author.
E-mail addresses: chenchuantong@sanken.osaka-u.ac.jp (C. Chen), l.liu@whut.edu.cn (L. Liu).

https://doi.org/10.1016/j.ceramint.2025.01.444
Received 25 October 2024; Received in revised form 8 January 2025; Accepted 24 January 2025
Available online 25 January 2025

of CuO produces a Cu layer that diffuses into the Al foil, resulting in robust Al/AlN joints [9]. Another approach involves the use of a transient eutectic liquid phase (TLP) in Al for joining AlN ceramics, offering a promising alternative [10,11]. Although active metal brazing or TLP techniques are widely applied for large-scale joining, including complex geometries and non-flat surfaces, reliable vacuum tight joints capable of withstanding high operating temperatures remain essential. High annealing temperatures lead to significant internal stress, especially at the metal/ceramic interface, as the joint cools to room temperature [12–14]. Furthermore, the vacuum and high-temperature processing conditions involved in these methods contribute to substantial equipment and fuel costs.

Extensive research has explored the application of Ag sinter paste as a promising alternative for attaching wide band-gap (WBG) die materials in high-temperature environments [15–18]. Ag sinter paste, typically fabricated by mixing Ag particles with a solvent, allows sintering at temperatures below 300 °C under low-pressure conditions. In SiC power modules, the die-attach structures formed using Ag sinter paste exhibit shear strengths exceeding 50 MPa, along with excellent thermal and electrical conductivity [19,20]. Ag sinter paste usually requires an Ag metallization layer or an Au metallization on both chip and substrate surfaces to form a strong joint, either through an Ag-Ag interface or Ag-Au inter-diffusion [21,22]. However, there are very limited reports on the direct bonding of Ag sinter paste to Al metal. Not only it is difficult to achieve Ag-Al diffusion at low temperatures, but also Al usually has a native oxide layer (Al_2O_3), which acted as a barrier layer to prevent interface inter-diffusion [23,24]. Similar to the challenges in directly bonding Ag sinter paste to Al, bonding Ag sinter paste to AlN ceramics is also difficult, particularly due to the limitations of the interfacial diffusion mechanism in low-temperature, low-pressure sintering processes [25,26]. Moreover, there have been few studies evaluating the bonding performance of Al/AlN using Ag sinter paste as an interlayer, especially with regard to the high-temperature reliability of these bonded structures.

In this study, we propose a novel technology for directly bonding bare Al to AlN ceramics using an interlayer of Ag sinter paste. The sintering process is conducted under low-temperature, pressure-less, and low-pressure conditions in an atmospheric environment. The resulting sintered Ag bonding layer achieves a thickness of less than 10 μm. The study evaluates the bonding characteristics and fracture behavior at different sintering temperatures. Advanced characterization techniques, including scanning electron microscopy (SEM), transmission electron microscopy (TEM), and energy dispersive spectroscopy (EDS), were employed to analyze the interfacial bonding mechanisms of the Ag sinter paste with Al and AlN substrates. A detailed investigation of the bonding mechanism at the Ag/Al interface is presented, with particular attention to the influence of the natural Al oxide layer (Al_2O_3). The diffusion behavior of Ag into Al and Al_2O_3 was compared using Molecular Dynamics (MD) simulations to elucidate the effect of the oxide layer on interface formation. To evaluate the structural reliability and fracture mechanisms under high-temperature conditions, the high-temperature reliability of the Al/AlN joint was examined through an aging test

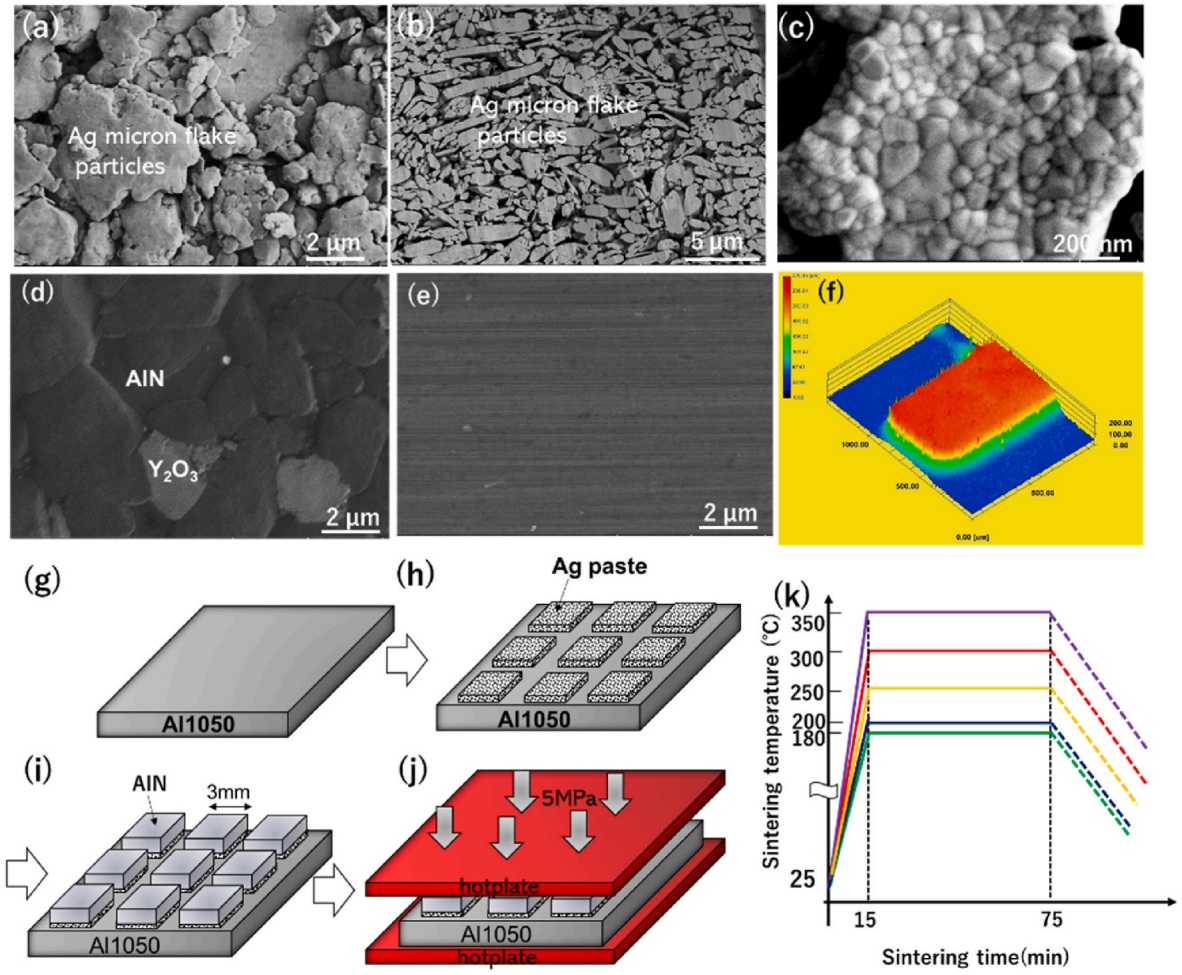

Fig. 1. (a) SEM image of Ag micron-sized flake particles, (b) the SEM cross-sectional image of Ag particles, (c) the modified view of Ag flake particle after heating for 5 min in 180 °C, (d) the AlN surface, (e) the SEM image of the Al surface, and (f) the 3D image of the Ag paste printed on Al surface, (g–j) joint process using the Ag paste, (k) sintering profile of the Ag paste for Al and AlN joining.

conducted at 300 °C for 500 h. The results provide insights into the robustness and durability of the bonding structure for high-temperature applications.

2. Methodology

2.1. Ag particle and paste

In this study, micron-sized Ag flake particles were selected as the Ag precursor, as illustrated in Fig. 1(a). These Ag flake particles were produced through a ball milling process using sub-micron spherical particles as the base material. The particles exhibited sizes ranging from 1 to 7 μm in the longitudinal direction, with an average thickness of approximately 300 nm. The cross-sectional view of the Ag particles, shown in Fig. 1(b), reveals that the particles are distributed randomly with varying sizes. During the ball milling process, dislocations formed within the particles, resulting in significant residual stress and strain. This phenomenon enables the Ag flake particles to undergo sintering at relatively low temperatures. Fig. 1(c) provides a magnified view of the Ag flake particles after heating at 180 °C for 5 min. It is evident that the Ag flake particles are composed of multiple nanoparticles. To facilitate low-temperature sintering, an organic solvent named CELTOL-IA was used to prepare the Ag sinter paste. CELTOL-IA promotes sintering of Ag particles at temperatures around 180 °C [27–29]. From the differential scanning calorimetry (DSC) curve, the solvent exhibited exothermic properties at approximately 250 °C [29]. The weight ratio of Ag particles to solvent was set to 13:1 to ensure the paste has a good printability with appropriate viscosity.

2.2. Al/AlN joint structure

The Al used in this study was commercial-grade Al1050, with an Al content exceeding 99.9 wt%. The AlN ceramic samples were obtained from Tokuyama Corporation, Japan. Before bonding, both the Al and AlN substrates were cleaned with acetone in an ultrasonic cleaner to ensure surface cleanliness. Fig. 1(d) shows the SEM image of the AlN surface, which exhibits a scaly appearance with a rough Yttrium oxide (Y_2O_3) layer visible. This Y_2O_3 layer acts as a sintering aid for the AlN ceramic. The surface roughness of the AlN substrate was measured to be 0.51 μm, with a fish-scale-like texture. The SEM image of the Al surface is shown in Fig. 1(e), while Fig. 1(f) presents a 3D image of the Ag paste printed onto the Al surface. To fabricate the sintered joint structure for bonding strength measurements, AlN samples with dimensions of 3 mm × 3 mm × 0.8 mm were prepared, alongside Al samples measuring 30 mm × 30 mm × 2 mm. The bonding process using Ag sinter paste is illustrated in Fig. 1(g–j). The Ag paste was screen-printed onto the Al substrate through a metal mask with a thickness of 50 μm, as depicted in Fig. 1(g). The AlN ceramic was then placed onto the Ag paste layer, as shown in Fig. 1(h) and (i). All specimens were sintered on a hotplate at temperatures ranging from 180 °C to 350 °C for 30 min in air. Two sintering approaches were employed: pressure-less sintering and sintering under a low pressure of 5 MPa. The heating process, from room temperature to the target sintering temperature, took 15 min, as illustrated in the temperature-time profile in Fig. 1(k).

2.3. Characterization

After the sintering process, the microstructure evolution of the Ag paste at various sintering temperatures and the morphologies of the sintered joint cross-sections were examined using field-emission scanning electron microscopy (FE-SEM, Hitachi SU8020, Hitachi). The sintered Ag paste was further characterized by X-ray diffraction (XRD) using a Rigaku SmartLab diffractometer (Akishima, Tokyo, Japan) with Cu Kα radiation at a scanning rate of 15°/min. The shear strength of the joint structures was evaluated using a die shear tester (DAGE, XD-7500) with a shear rate of 50 μm/s. The height for the shear test was set to 20 μm, corresponding approximately to the thickness of the sintered Ag paste. To ensure statistical accuracy, five specimens were tested for each condition, and the average shear strength was calculated. For cross-sectional analysis, the joints were prepared using an ion-milling polishing system (IM4000, Hitachi High-Technologies, Japan). Detailed interface observations were conducted using transmission electron microscopy (TEM, JEM-ARM200F, JEOL Ltd.), equipped with energy-dispersive spectroscopy (EDS). Cross-sectional samples of the sintered AlN/Al joint were prepared using a focused ion beam (FIB, FIB-2100, Hitachi). High-temperature reliability testing of the Al/AlN joint structures was performed by subjecting the samples to aging at 300 °C for 500 h to assess their durability under prolonged thermal exposure.

2.4. Molecular dynamics simulation

To understand the interface bonding mechanism of Ag pastes on the substrates, we employed molecular dynamic (MD) simulations to investigate the interfacial diffusion behaviors of Ag/Al and Ag/Al_2O_3 at 300 °C. The geometries for the Ag/Al and Ag/Al_2O_3 were modeled by Materials Studio (MS) and subsequently processed in the Large Scale Atomic/Molecular Parallel Simulator (LAMMPS), with the corresponding geometric data files generated for analysis. Finally, the visualization of simulation results was carried out by the OVITO software.

The MD models of Ag/Al and Ag/Al_2O_3 are depicted in Fig. 2. The simulation box for the Ag/Al model measured approximately 50 × 50 × 120 Å and contained 18750 atoms, while the simulation box for the Ag/Al_2O_3 model was about 53 × 51 × 104 Å, containing 23188 atoms. The number of Ag atoms in the Ag/Al model was kept roughly equivalent to that in the Ag/Al_2O_3 models. Periodic boundary conditions were applied in the x, y, and z directions to simulate an infinite lattice. For diffusion at the Ag/Al interface, the interaction between Ag and Al atoms was described using the Embedded Atom Method (EAM) potential, a fitted potential function that has been widely used in modeling systems involving metals for a wide range of metals, including the two metals used in this simulation [30]. The Ag/Al_2O_3 system employed the EAM potential, charge optimized many-body (Comb3) potential and modified embedded atom method (Mean) potential to describe the interatomic interactions.

Before initiating the simulation, an energy minimization was performed by the conjugate gradient algorithm, while relaxation process was then conducted within the canonical (NVT) ensemble for 5 ps to allow this system to reach thermal equilibrium. After relaxation, the diffusion process was simulated at 300 °C by an isothermal isobaric (NPT) ensemble to allow complete diffusion of the atoms. This ensured that both temperature and pressure conditions remained stable while promoting atomic diffusion across the interface.

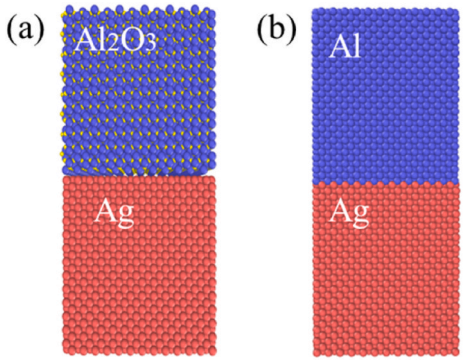

Fig. 2. MD models of: (a) Ag/Al_2O_3 interface, (b) Ag/Al interface.

3. Results and discussion

3.1. Sintered Ag paste

To understand the sintering behaviors of Ag paste, the morphology evolution at different sintering temperatures was investigated. Fig. 3 (a–d) presents SEM images of the Ag paste sintered at 180 °C, 200 °C, 250 °C, and 300 °C for 30 min in air. At the lower temperature of 180 °C, the microstructure of the Ag paste becomes apparent as the solvents evaporate or burn off. At this stage, necking at the particle interfaces begins, though the initial Ag flake shape remains observable. As the sintering temperature increases to 200 °C, the system transitions to a lower energy configuration, allowing for the rearrangement of Ag particles and promoting more pronounced necking growth between them. Despite the compactness of the sintered Ag paste at this stage, continuous pores remain due to incomplete decomposition of the solvent coating on the Ag particles' surface. At a sintering temperature of 250 °C, a smoother surface and a more compact microstructure are observed. The morphology evolution observed at these temperatures aligns closely with results from previous studies [31–34]. When the sintering temperature is further increased to 300 °C, the Ag particles bond tightly, resulting in a denser structure with only a few remaining pores. The thermal and electrical properties of sintered Ag are significantly influenced by its microstructure, with denser Ag structures providing better thermal and electrical conductivity [35,36].

Fig. 3(e) shows the X-ray diffraction (XRD) curves of the Ag paste before and after sintering at different temperatures. The initial Ag particles, both pre- and post-sintering, exhibit a polycrystalline structure, with the Ag (111) plane displaying the highest diffraction peak as reported in previous study [34]. Usually, the intensity of the peaks in an XRD pattern is influenced by the amount of crystalline material present. Higher crystallinity means a more ordered atomic arrangement, which results in sharper and more intense diffraction peaks. In this study, with the temperature increase, the Ag (111) diffraction peak becomes more intense, indicating an increase in crystallinity. In addition, comparing with initial Ag particles, an increase in temperature can cause thermal expansion or contraction of the crystal lattice, thereby altering the lattice spacing and resulting in a shift of the diffraction peak positions after sintering.

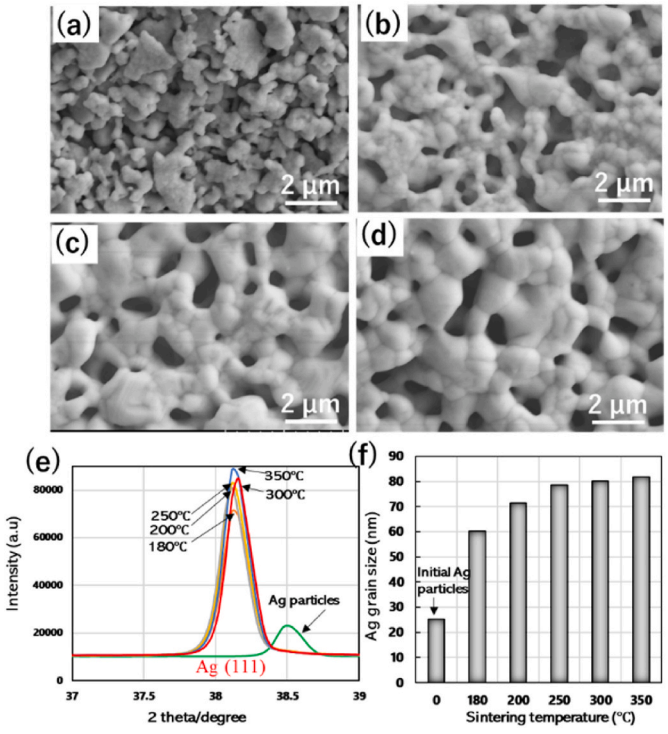

Fig. 3. SEM image of Ag particles sintering at (a) 180 °C, (b) 200 °C, (c) 250 °C, and (d) 300 °C for 30 min, (e) XRD curves of Ag paste before and after sintering at different temperatures at the Ag (111) diffraction peak, (f) Ag crystallite size evolution at different sintering temperatures.

Fig. 3(f) illustrates the average crystallite size of the Ag paste before and after sintering at various temperatures, measured through XRD analysis. The initial crystallite size of the Ag flake particles was approximately 30.7 nm, which significantly increased to 60.2 nm after sintering at 180 °C. This indicates that necking between Ag particles had already commenced at this lower temperature. The crystallite size further increased to 78.6 nm after sintering at 250 °C and to 81.1 nm at 350 °C, demonstrating that higher sintering temperatures promote crystallite growth.

3.2. Characterization of Al/AlN sintered joints

3.2.1. Cross section of Al/AlN sintered joint

Fig. 4(a) presents the cross-sectional SEM image of the Al/AlN joint structure fabricated using Ag sinter paste at a sintering temperature of 200 °C without applied pressure. The sintered Ag paste exhibits a micron-sized porous network structure, rather than large voids in the sintered Ag layer. The porosity of the sintered Ag paste was measured as 39 %, determined using the IPWin4-Image analysis software based on the SEM image. Fig. 4(b) and (c) show the bonding characteristics at the AlN/sintered Ag paste layer interface and the sintered Ag paste layer/Al substrate interface, respectively. In both cases, the sintered Ag paste forms strong interfacial bonds with the AlN and Al through pronounced necking growth of Ag grains. These results confirm that reliable bonding between Ag/AlN and Ag/Al can be achieved under low-temperature, pressure-less conditions.

Fig. 4(d) illustrates the cross-section of the Al/AlN joint structure sintered at 300 °C. At this higher temperature, the porosity of the sintered Ag paste decreases to 35 %, attributed to enhanced necking growth of Ag grains. Fig. 4(e) and (f) demonstrate that the interfacial necking between the sintered Ag paste and both the AlN and Al substrates is further improved at 300 °C, indicating better bonding quality at elevated sintering temperatures. Fig. 4(g–j) display the EDS elemental mapping of the cross-section of the Al/AlN joint structure sintered at 200 °C, corresponding to the SEM image in Fig. 4(b). The EDS analysis reveals no significant chemical reactions or formation of new intermetallic compounds (IMCs) at the interfaces. The reason and mechanism for the formation of this interface at low temperature may be different from the traditional metal-ceramic diffusion at high temperature and high vacuum, which will be analyzed in a later article.

Fig. 5(a) and (d) show SEM images of the cross-sections of the AlN/Al joint structure under different sintering temperature under a pressure of 5 MPa. Compared to pressure-less sintering, the sintered Ag paste exhibits a denser microstructure with reduced porosity when pressure is applied during the sintering process. The application of pressure significantly influenced the necking growth of Ag particles during sintering. Fig. 5(b) and (c) illustrate that even at a sintering temperature of 200 °C, robust necking growth is observed at the AlN/Ag interface and the Ag/Al substrate interface, respectively. When the sintering temperature increased to 300 °C, the microstructure became very denser, with lower porosity and more extensive grain necking between Ag particles. Fig. 5(g) presents the interface necking ratio of the Al/AlN joint structure fabricated using Ag sinter paste at sintering temperatures of 200 °C and 300 °C under a pressure of 5 MPa. This data is compared to the interface necking ratio obtained in pressure-less sintering conditions at the same temperatures. The interface necking ratio serves as a quantitative measure of the degree of connection between the sintered Ag particles and the AlN or Al substrate, providing insight into the bonding quality. The interface necking ratio was calculated using the following equation [37,38]:

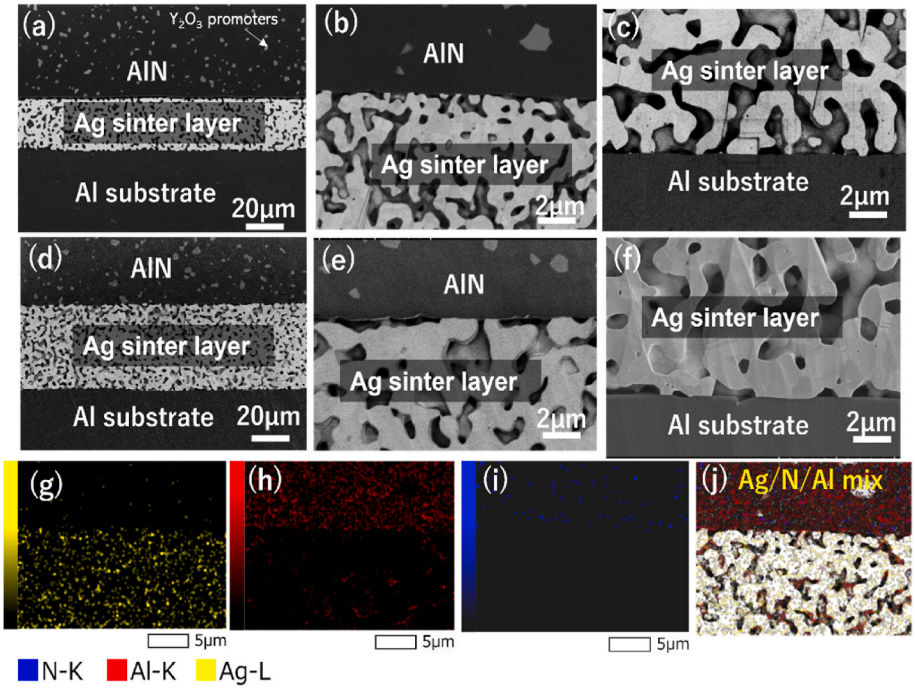

Fig. 4. (a) Shows the SEM image of the cross section of the Al/AlN joint structure using Ag sinter paste at a 200 °C temperature in pressure-less conditions, (b) the bonding interfaces between AlN and the sintered Ag, (c) the interface between sintered Ag paste and the Al substrate interface, (d) the cross-section of the Al/AlN joint structure at 300 °C, (b) the bonded interfaces AlN/Ag, (c) the bonded interface Ag/Al at 300 °C, (g–i) EDS element mapping of the cross-section of the Al/AlN joint structure at 200 °C, and (j) the mixed-element mapping.

$$\delta = \frac{\Sigma\, l_{connected}}{l_{total}} \tag{1}$$

where δ is the connected ratio, l total length of the interface, and Σl connected is the total length of bonded location between the interface. The results indicate that applying pressure during sintering significantly enhances the necking growth and bonding quality, particularly at elevated sintering temperatures. Interestingly, the interface necking ratio between the AlN and the sintered Ag was consistently lower than that between the sintered Ag and the Al substrate. This disparity could be attributed to two factors: firstly, during the sintering process, the AlN substrate was positioned on the upper side of the Ag paste. This positioning may have influenced the evaporation rate and temperature distribution of the organic solvent, which differed from the lower side where the Al substrate was located. Secondly, the chemical and physical reactions occurring at the Ag/AlN interface during sintering may differ from those at the Ag/Al interface, potentially leading to variations in necking growth.

Fig. 5(h) illustrates the porosity evolution of the sintered Ag paste under different sintering conditions and temperatures. Unlike the trend observed in the interface necking ratio, the porosity decreased with increasing sintering temperatures and the application of pressure. This reduction in porosity indicates that the necking growth of Ag particles was significantly enhanced at higher temperatures and with the application of pressure during sintering [39,40].

3.2.2. Shear strength of Al/AlN joints

Following the sintering process, the shear strength of the die-attached structure was evaluated. Fig. 6 illustrates the shear strength of the AlN/Al joint structure under both pressure-less and low pressure conditions across various sintering temperatures. The results show a positive correlation between sintering temperature and shear strength. Under pressure-less sintering, the shear strength reached 20.3 MPa at 350 °C. However, a significant improvement was observed under low-pressure sintering at 5 MPa, where the shear strength reached 40.5 MPa at 300 °C. This shear strength surpasses the values achieved by traditional methods for bonding Al to AlN ceramics, including the active metal method in transient liquid phase (TLP) bonding [41–43] and the use of a CuO interlayer [9]. Furthermore, like the active metal and TLP bonding techniques, Ag sinter paste provides versatility for joining. It facilitates large-scale bonding processes, accommodating intricate geometries and surfaces beyond simple flat configurations.

Fracture surface morphologies of the AlN/Al joint sintered under three conditions of 200 °C pressure-less, 200 °C at a low pressure of 5 MPa, and 300 °C under a low pressure of 5 MPa are shown in Fig. 7(a), (b), and (c), respectively. At 200 °C without pressure, the fracture surface primarily exhibits a bare Al substrate with scattered sintered Ag particles, as seen in Fig. 7(d). The fracture occurred along the bonded interface of the sintered Ag and Al substrate. While much of the sintered Ag exhibited brittle failure, some areas demonstrated tight bonding to the Al substrate with slight ductile deformation after the shear test. This indicates the potential for forming a robust Ag/Al interface at low temperatures, even without pressure-assisted sintering.

When sintered at 200 °C under low pressure, fracture initiation occurred at the sintered Ag and AlN interface. It then transitioned to the sintered Ag and Al substrate interface at the bonded area's center, as shown in Fig. 7(b). The fracture surface displayed significant ductile deformation of the sintered Ag, particularly at the interface with AlN, indicating a well-bonded network structure (Fig. 7(e)). At a higher sintering temperature of 300 °C under low pressure, fractures predominantly occurred at the interface between AlN and the sintered Ag layer (Fig. 7(c)). The ductile fracture characteristics on this surface became more prominent, further highlighting the improved bonding strength and ductility at elevated sintering temperatures. Fig. 7(g–i) present schematic diagrams of the fracture modes during shear testing for the three sintering conditions, providing a visual representation of the fracture initiation and propagation paths under varying temperature and pressure conditions.

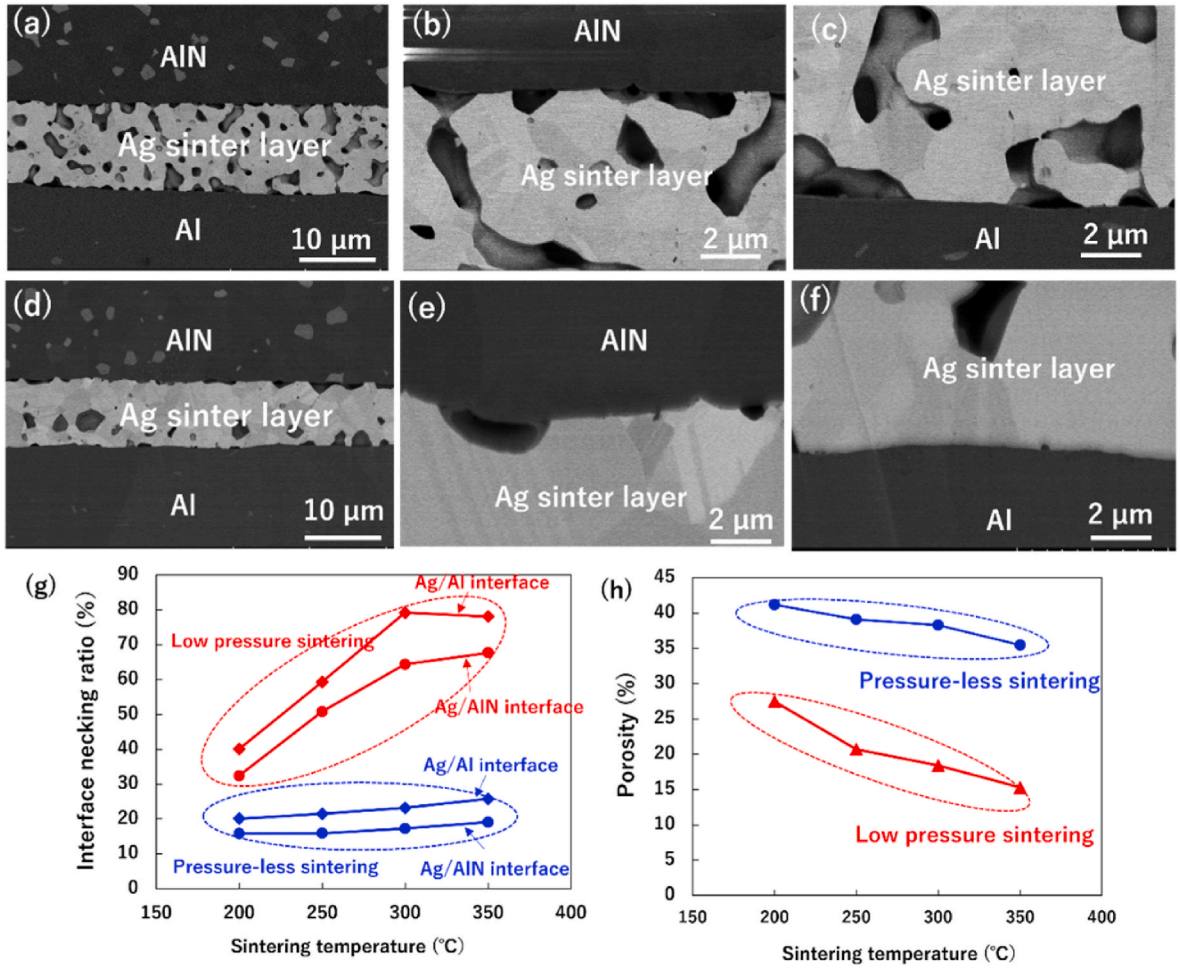

Fig. 5. (a) SEM image showing the cross-section of the AlN/Al joint structure using Ag sinter paste at a sintering temperature of 200 °C and pressure of 5 MPa, (b) the magnified view of the interface between AlN and sintered Ag, (c) the magnified view of the interface between sintered Ag and Al, (d) AlN/Al joint structure at a sintering temperature of 300 °C and pressure of 5 MPa, (e) the interface between AlN and sintered Ag, (f) the interface between sintered Ag and Al, (g) the interface necking ratio, and (h) the porosity evolution of the Al/AlN joint structure using Ag sinter paste at different sintering temperatures in both pressure and pressure-less cases.

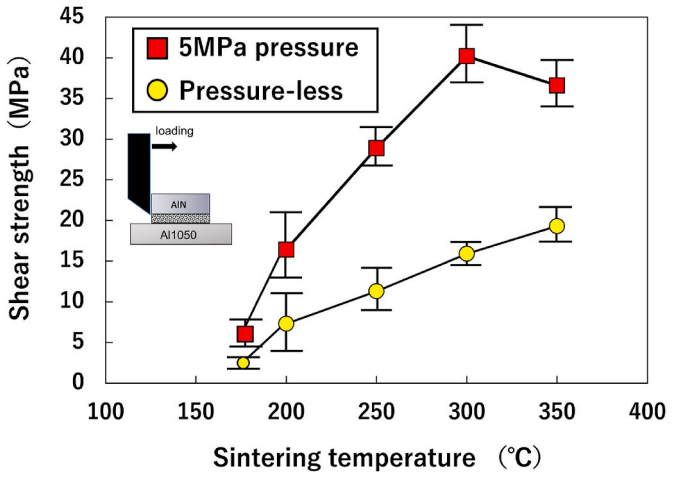

Fig. 6. Shear strength of the AlN/Al joint structure without pressure and with low pressure at different sintering temperatures.

3.2.3. *Bonded interface analysis*

TEM analysis was performed to investigate the interfaces between sintered Ag and Al, as well as between sintered Ag and AlN, revealing insights into the bonding mechanisms during low-temperature sintering. Fig. 8(a) illustrates the tight adhesion of the sintered Ag layer to the Al surface. A magnified view of the bonding interface in Fig. 8(b) reveals a bright intermediate layer approximately 5 nm thick between Ag and Al. Selected area electron diffraction (SAED) pattern in Fig. 8(c), (d), and (e) respectively correspond to specific spots a, b, and c in Fig. 8(b). The SAED pattern at Spot a exhibits a well-crystallized Al structure. Spot b confirms the presence of an amorphous alumina (Al_2O_3) layer, which is the natural oxide layer and inherent on the Al surface, showing no lattice fringes. Spot c shows an irregular pattern due to the polycrystalline structure of sintered Ag. Based on the magnified view, it was confirmed that Ag and Al intimately adhere to the alumina layer without any voids or delamination. Energy-Dispersive X-ray Spectroscopy (EDS) mapping, shown in Fig. 8(f–i), further corroborates the intimate bonding between Ag and Al. This strong adhesion is attributed to the excellent sinter ability of Ag paste at low temperatures. Interestingly, no significant inter-diffusion between Ag and Al was detected, indicating that the bonding is primarily governed by the tight adhesion of the Ag layer to the amorphous Al_2O_3 layer present on the Al substrate surface [44,45].

Fig. 9(a) shows a TEM image of the bonded interface between the sintered Ag and AlN. The porous structure of the sintered Ag is evident, with some pores observed near the interface. A magnified view reveals that the sintered Ag, with its polycrystalline structure, is well attached to the AlN substrate.

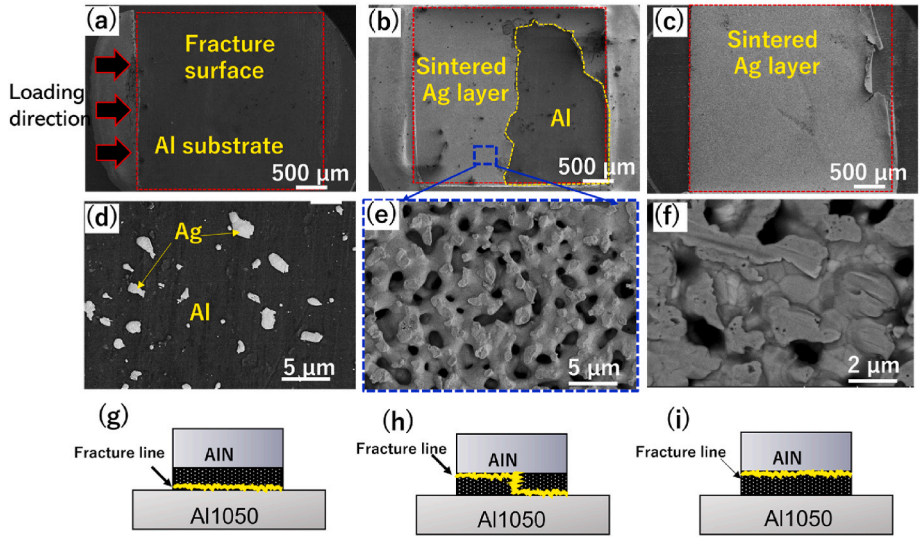

Fig. 7. Fracture surface morphologies of AlN/Al joint sintering at (a) 200 °C in pressure-less conditions, (b) 200 °C at a low pressure of 5 MPa, and (c) 300 °C at a low pressure of 5 MPa. (d), (e), and (f) show the magnified view of the fracture surface corresponding to (a), (b), and (c), respectively. (g), (h), and (i) show the schematic diagram of the fracture mode during the shear test.

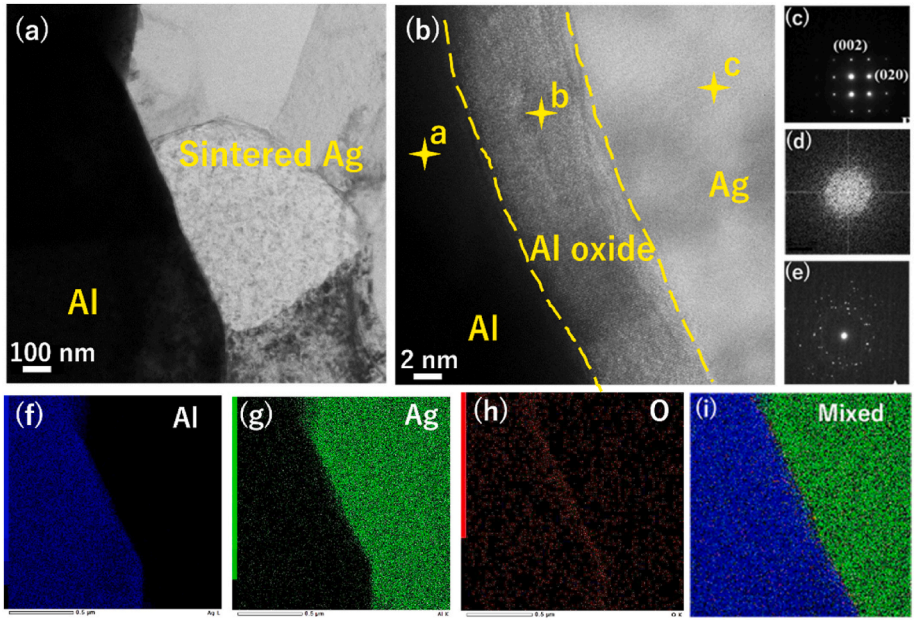

Fig. 8. (a) Bonded interface between Al and sintered Ag, (b) magnified view of the interface, (c–e) the SAED pattern of Al, Al oxide layer, and sintered Ag, respectively, (f–i) the EDS element mapping of Al, Ag, O, and the mixed element, respectively.

In Fig. 9(b), a closer examination of the Ag/AlN interface shows no significant reactants, making it difficult to detect elemental diffusion between Ag and AlN. Additionally, SAED patterns in Fig. 9(c) and (d) confirm the presence of Ag (200) and AlN (0001) textures, respectively. Based on the TEM interface observations and SAED pattern analyses, an interfacial orientation relationship of Ag (200)//AlN (0001) was identified. However, since TEM examines a very small localized interface, further extensive observations and research are required.

Previous studies, supported by atomistic simulations using density functional theory (DFT), have suggested the feasibility of a coherent Ag/AlN interface [46,47]. The interface formation mechanism is discussed in this study. The TEM image in Fig. 9(e) further highlights the porous structure of the sintered Ag. Fig. 9(f) reveals the presence of numerous small Ag particles, ranging in size from several tens of nanometers, within the porous structure of the sintered Ag, particularly near the Ag necking locations. Additionally, small Ag particles are observed to form at the AlN interface, as shown in Fig. 9(g). These aggregated Ag particles on the AlN surface promote enhanced neck formation at the interface, contributing to a denser structure. It has been reported that Ag flakes exhibit superior sinter ability due to the release of residual stress and the formation of Ag nanoparticles [48,49]. These nanoparticles, with their high surface energy, enhance wettability on the AlN substrate.

Furthermore, in some locations, a thin Al oxide layer was identified on the AlN substrate. The interface bonds are formed through Ag diffusion into the Al oxide layer, similar to the bonding mechanism observed for the Ag-Al interface. Since AlN samples are stored and sintered in air, localized oxygen infiltration results in the formation of Al oxide on the surface.

The generation of Ag nanoparticles is also evident in SEM images after sintering Ag flake paste at 200 °C for 5 min, as shown in Fig. 10(a).

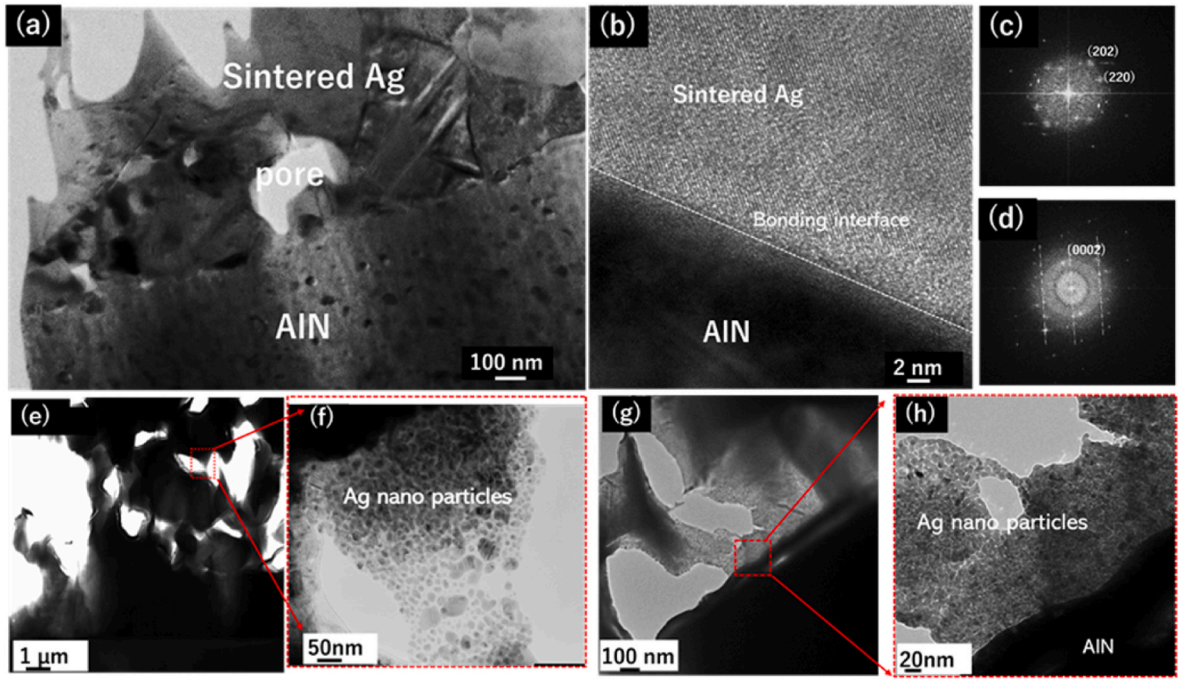

Fig. 9. (a) TEM image of the bonded interface between sintered Ag and AlN, (b) the magnified view of the bonded interface, SAED pattern of (c) Ag and (d) AlN, (e) TEM image of sintered Ag porous structure, (f) Ag nanoparticle generation in the sintered Ag, (g) Ag nanoparticle generation at the AlN interface, and (h) magnified view of the interface.

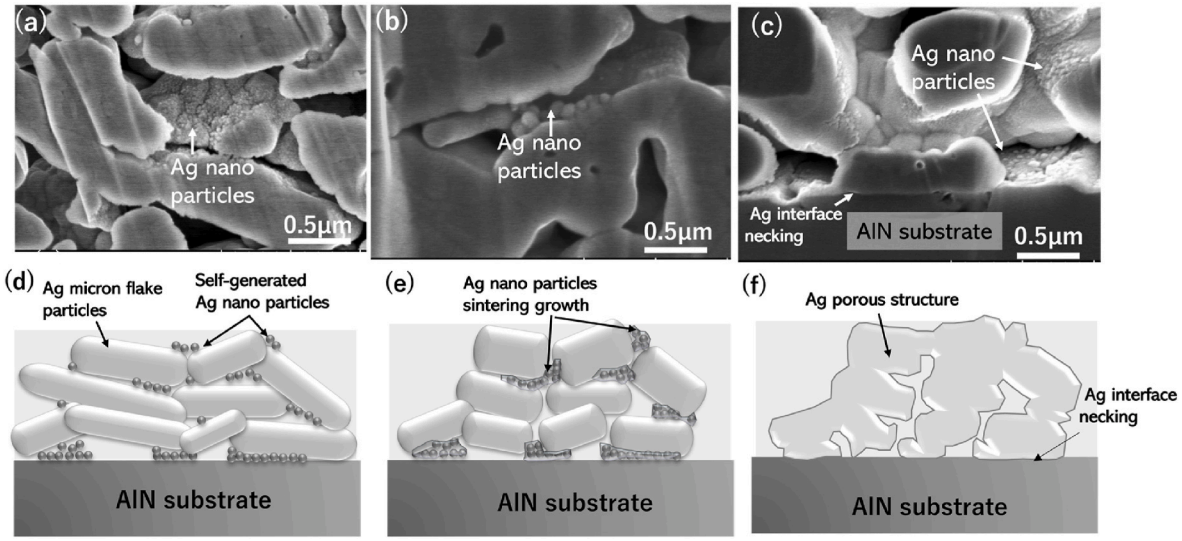

Fig. 10. (a) SEM image after the Ag flake paste was sintered at 200 °C for 5 min, (b) 10 min, (c) Cross section of sintered Ag paste on AlN substrate at 200 °C for 10 min, (d) Schematic diagram showing the generation of small Ag nanoparticles, (e) Growth of small Ag particles, and (f) Effect on Ag flake particle necking and interface necking formation.

These small Ag particles completely cover the surfaces of Ag flake particles and fill the gaps between them. The formation of such nanoparticles is unlikely to result from the sample preparation process; however, the exact physical mechanism behind their generation remains unclear. When the sintering time is extended to 10 min at 200 °C, as shown in Fig. 10(b), the size of the Ag particles increases. Notably, the growth of these small Ag nanoparticles significantly enhances interface bonding due to their high surface energy. Fig. 10(c) illustrates the cross-section of sintered Ag paste on an AlN substrate after 10 min of sintering at 200 °C, revealing that an interface has already formed. Bonding ceramic and metal through inter-diffusion, especially at low temperatures and over a short time, is inherently challenging. However, the formation of a robust interface in this case is attributed to the generation of small Ag nanoparticles, as corroborated by TEM and SEM observations. These nanoparticles play a pivotal role in bonding with both Al and AlN, enabling tight interconnection due to their high surface energy. This phenomenon results in excellent interface bonding during the sintering process. Fig. 10(d–f) present schematic diagrams illustrating the generation and growth of small Ag nanoparticles, their contribution to necking formation among Ag flake particles, and their effect on interface bonding.

3.3. Molecular dynamics (MD) simulation

To gain a deeper understanding of the diffusion and bonding behavior of sintering Ag on Al and Al_2O_3 substrates, MD simulations were conducted for the Ag/Al_2O_3 and Ag/Al interfaces. The atomic diffusion behavior of the Ag/Al and the Ag/Al_2O_3 interfaces at different time intervals at 300 °C were illustrated in Fig. 11. Atoms near the interface migrate to the other side by atomic diffusion, eventually forming a neck structure. The process also generates grain boundary diffusion and dislocations that promotes interconnections. In general, the atomic diffusion behaviors at both the Ag/Al_2O_3 and Ag/Al interfaces are not pronounced. Particularly, there is only minimal atomic diffusion at the Ag/Al interface, while the diffusion at the Ag/Al_2O_3 interface is slightly obvious compared to the Ag/Al interface. This phenomenon is highly likely due to the presence of oxygen, which promotes atomic diffusion at the interstitial sites of the lattice [50].

Fig. 12 presents the diffusion depth and the mean square displacement (MSD) curves for the Ag/Al_2O_3 and Ag/Al interfaces. The MSD was calculated to quantitatively describe the diffusion characteristics, which can be as [51]:

$$\mathrm{MSD} = <r^2(t)> \geq \frac{1}{N}\sum_{i=1}^{N}\left(|r_i(t) - r_i(0)|^2\right) \quad (2)$$

Where $r_i(t)$ represents the position of the atom at time t, and $r_i(0)$ denotes the position of the atom in its initial state.

Notably, the diffusion depth of Ag into the Al_2O_3 and Al substrates at 50 ps are 21.22 Å and 9.3 Å as shown in Fig. 12(a) and (b), respectively. This agrees with the observation in Fig. 11, indicating that Al_2O_3 moderately promote faster and more diffusion of Ag atoms than Al. On the other hand, according to their MSD curves in Fig. 12(c) and (d), in the initial stage before 5 ps, the atomic diffusion in the Ag/Al system seems to be slightly stronger than the diffusion behavior at the Ag/Al_2O_3 interface. Afterwards, the overall MSD in the Ag/Al_2O_3 system keeps increasing linearly over time with a steeper slope, while the MSD of the Ag/Al system quickly drops and remains almost flat over time with a minimal slope. The slope of the MSD curves obtained from the linear fit are denoted as 3.3×10^{-6} Å^2/fs for the Ag/Al model and 3.36×10^{-5} Å^2/fs for the Ag/Al_2O_3 model, respectively. This indicates that the initial diffusion of Ag atoms in the Ag/Al_2O_3 system is hindered by higher resistance, as the bonding between Ag and O sites is stronger, resulting in a higher diffusion barrier. In contrast, the weaker bonding between Ag and Al sites leads to a lower diffusion barrier, allowing for a relatively faster diffusion rate on the Al_2O_3 surface over time [52]. Moreover, the higher diffusion depth of at 21.22 Å the Ag/Al_2O_3 interface can be attributed to the fact that the presence of Ag in Al_2O_3 increases charge trapping and allows low-valence cations can occupy interstitial sites [53].

As for Ag/Al system, its interfacial diffusion is limited with a smaller diffusion depth of 9.3 Å. This is because Al and Ag share the same bulk structure (FCC) and have a small lattice mismatch of 1 %, resulting in better atomic compatibility and lower interfacial energy [54]. Although higher temperatures can reduce the diffusion activation energy, the activation energy required for Ag to diffuse into Al at 300 °C still remains high due to the size difference between Ag and Al atoms. This means that Ag atoms need more energy to overcome the barriers during the diffusion process and achieve effective diffusion.

3.4. High-temperature reliability test

The high-temperature reliability test involved aging the AlN/Al joint structures, which were sintered at 300 °C under a pressure of 5 MPa and then aged at 300 °C for 500 h. Fig. 13(a)–(d), and (g) illustrate the cross section of the AlN/Al joints after aging for 0, 100, and 500 h, respectively, at 300 °C. These cross-sectional images of the AlN/Al joints show a well-bonded structure where the chip side and substrate side are bonded through sintered Ag. As the aging storage time increased, the Ag exhibited a coarsened structure with larger bonding necks and pores resulting from the growth of Ag grains at high temperature. Notably, some pores extended from the top AlN to the bottom Al substrate. The magnified images of the bonded interface between sintered Ag and Al, presented in Fig. 13(b)–(e), and (h), correspond to Fig. 13(a)–(d), and (g), respectively. Throughout the high-temperature aging process, no Ag-Al intermetallic compound (IMC) was detected at the bonding line

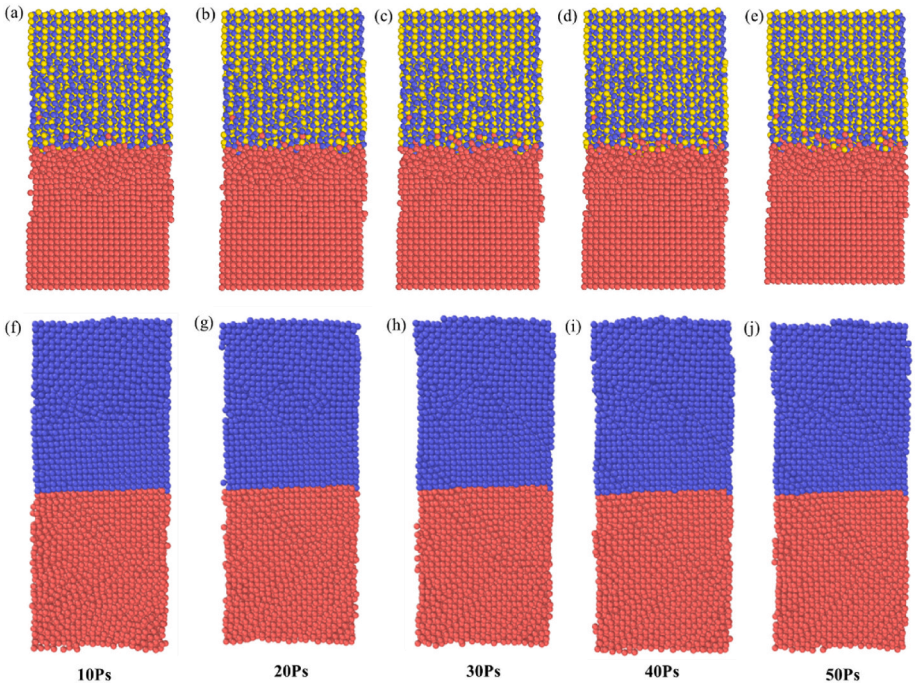

Fig. 11. Atomic diffusion behaviors of Ag/Al and Ag/Al_2O_3 interfaces for different times at 300 °C: (a) Ag/Al_2O_3-10ps, (b) Ag/Al_2O_3-20ps, (c) Ag/Al_2O_3-30ps, (d) Ag/Al_2O_3-40ps, (e) Ag/Al_2O_3-50ps, (f) Ag/Al-10ps, (g) Ag/Al-20ps, (h) Ag/Al-30ps, (i) Ag/Al-40ps, (j) Ag/Al-50ps.

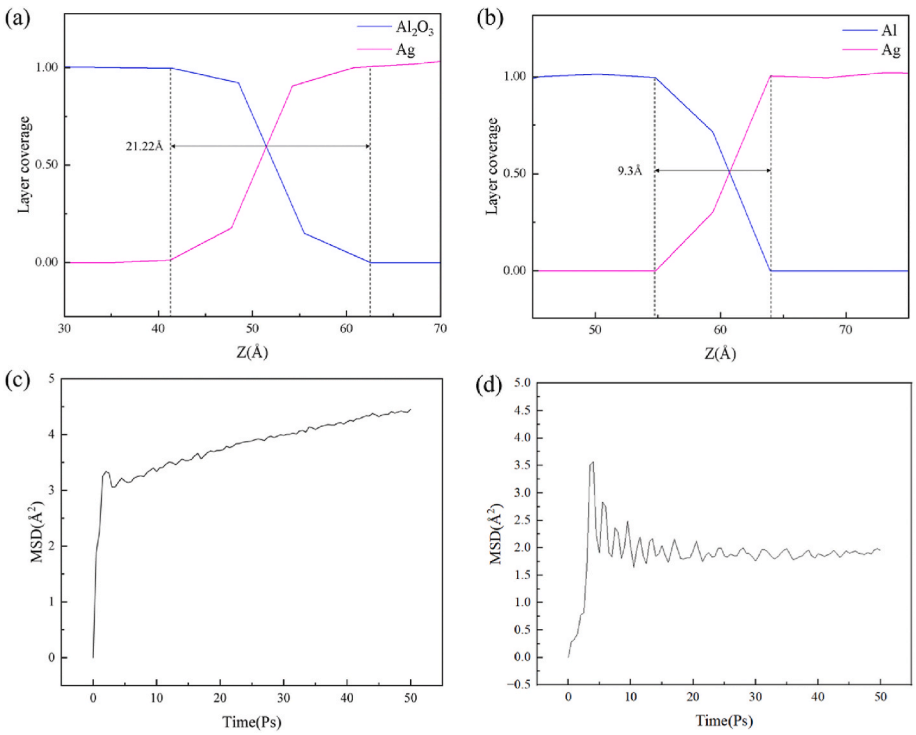

Fig. 12. (a) Diffusion depth for Ag/Al_2O_3 system, (b) diffusion depth for Ag/Al system, (c) MSD curves of Ag/Al_2O_3 system, (d) MSD curves of Ag/Al system.

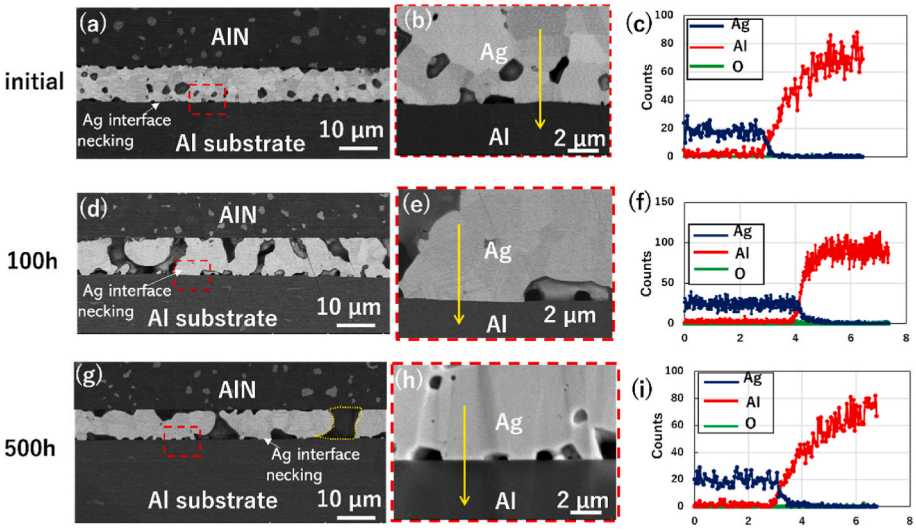

Fig. 13. (a) Initial AlN/Al joint, (b) Bonded interface between sintered Ag and Al, and (c) EDS line-element analysis; AlN/Al joint after aging at 300 °C for (d) 100 h and (g) 500 h, (e) and (h) Bonded interface between sintered Ag and Al after aging corresponding to (d) and (g), respectively, (f) and (i) EDS line analysis after aging for 100 h and 500 h, respectively.

according to the contrast in the SEM images. Ag maintains a tight adhesion to the Al surface via the bonding necks without any observable interface cracks or delamination even after 500 h of aging at 300 °C. Moreover, EDS line analysis (see Fig. 13(c)–(f), and (i)) confirmed that there was no clear Ag-Al inter-diffusion or growth of the oxide layer during high-temperature aging. This suggests that the interface remains stable, ensuring the reliability of the joint structure under prolonged thermal exposure.

The shear strength of the AlN/Al joint structure after aging was evaluated using a die shear tester. While the shear strength decreased with increasing aging time, it remained at 24.1 MPa even after 500 h of aging. Considering the aging temperature of 300 °C, which significantly exceeds those used in current industry standards for DBA or DBC substrate reliability tests, this level of shear strength is deemed acceptable. The observed reduction in shear strength is attributed to the coarsening process, which results in a larger bonding neck and a reduced connection area between the sintered Ag and the Al and AlN substrates.

The evolution of the interface necking ratio before and after aging is shown in Fig. 14(b). It indicates an approximate 50 % reduction in the interface necking ratio for both interfaces compared to the initial value. Fig. 14(c) presents the fracture surface of the joint structure after 100 h of aging, while Fig. 14(d) provides a magnified view of this fracture surface. Fractures predominantly occurred at the interface between the sintered Ag and AlN. After 100 h of aging, the significant decrease in

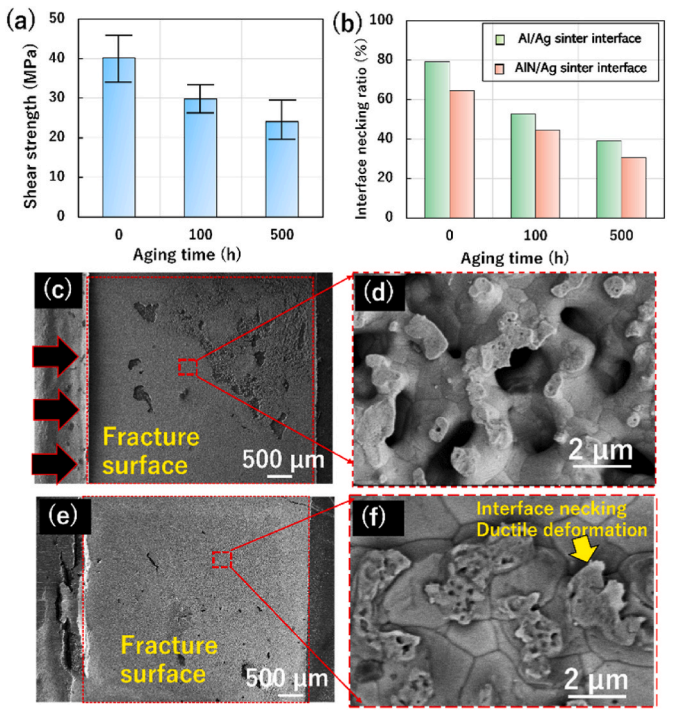

Fig. 14. (a) Shear strength of Al/AlN before and after aging, (b) Evolution of the interface necking ratio before and after aging, (c) Fracture surface of the joint structure after aging for 100 h, (d) Magnified view of the fracture surface, (e) Fracture surface of the joint structure after aging for 500 h, and (f) Ductile deformation of Ag necking.

shear strength suggests that the joint strength was insufficient to induce plastic deformation of the sintered Ag at the bonding interface, leading to brittle fracture. Fig. 14(e) shows the fracture surface after 500 h of aging, with fractures still occurring at the interface between the sintered Ag and AlN. Additionally, Fig. 14(f) highlights the ductile deformation of Ag necking observed after the shear test, indicating that good bonding between the sintered Ag and AlN persists even after 500 h of aging at 300 °C. However, since the shear strength of the joint decreased after 500 h of aging, the observed ductile necking of the sintered Ag may be attributed to the coarsening of the microstructure in this case.

4. Conclusions

In this study, we successfully achieved Al/AlN interface bonding using Ag sinter paste starting at a temperature of 180 °C. The interface formation mechanism was analyzed through Transmission Electron Microscopy (TEM) observations and Molecular Dynamics (MD) simulations. Additionally, the interface reliability of the Al/AlN joint was evaluated during high-temperature aging tests. This Ag sinter paste presents a strong alternative for directly bonding metals to ceramics, offering a promising solution for applications requiring reliable metal-ceramic joints. This innovative technology holds significant potential for applications demanding durable and reliable aluminum-to-ceramic bonds, particularly in environments involving low processing temperatures and extended high-temperature exposure. The key findings of this study are summarized as follows:

(1) The shear strength of the Al/AlN joint was influenced by sintering conditions, particularly by the application of pressure, which significantly improved interface necking and shear strength. A maximum shear strength of 40.5 MPa was achieved at a sintering temperature of 300 °C under 5 MPa pressure. This sintering temperature is notably lower than aluminum's melting point (660 °C), highlighting the energy efficiency of this method.

(2) TEM analysis revealed that during sintering, Ag particles adhere to and interact with the natural aluminum oxide layer (Al_2O_3) and AlN. This interaction results in a porous structure within the bonding layer at low sintering temperatures. The generated Ag nanoparticles play a pivotal role in bonding with both Al and AlN, enabling tight interconnection due to their high surface energy.

(3) MD simulations provided insights into the bonding mechanisms at the Ag/Al and Ag/Al_2O_3 interfaces. The results indicated that Ag diffuses into Al_2O_3 at a moderately faster rate than Al, enhancing bonding efficiency through improved interface formation facilitated by the Al_2O_3 layer.

(4) The bonded Al/AlN structure underwent aging at 300 °C for 500 h. Despite microstructural evolution within the bonding layer, the shear strength remained at 24.1 MPa even after 500 h of aging. No Ag-Al intermetallic compound (IMC) was detected at the bonding line according to the contrast in the SEM images and EDS analysis. Ag maintains a tight adhesion to the Al surface via the bonding necks without any observable interface cracks or delamination even after 500 h, demonstrating exceptional stability and reliability under high-temperature conditions.

CRediT authorship contribution statement

Chuantong Chen: Writing – review & editing, Writing – original draft, Supervision, Resources, Project administration, Funding acquisition. **Li Liu:** Validation, Supervision, Methodology, Formal analysis. **Fupeng Huo:** Methodology, Investigation. **Dongjin Kim:** Methodology, Formal analysis, Data curation. **Sangmin Lee:** Resources, Methodology, Data curation. **Wanli Li:** Methodology, Investigation. **Katsuaki Suganuma:** Validation, Supervision.

Declaration of interest Statement

We confirm that this manuscript has not been published elsewhere and is not under consideration in whole or in part by another journal. All authors have approved the manuscript and agree with submission to Ceramics International. All data is true and reliable. The authors have no conflicts of interest to declare.

Acknowledgement

This work was supported by a project (JPNP14004, Grant Number 21502156–0) commissioned by the New Energy and Industrial Technology Development Organization (NEDO) and JSPS KAKENHI (Grant Number 22K04243), and JST (Grant number JPMJSF23DB). This study was also partly supported by research grant from Japan Power Academy.

References

[1] K. Shenai, M. Dudley, R.F. Davis, Current status and emerging trends in wide bandgap (WBG) semiconductor power switching devices, ECS J. Solid State Sci. Technol. 2 (2013) N3055–N3063.
[2] W.H. Tuan, S.K. Lee, Eutectic bonding of copper to ceramics for thermal dissipation applications: a review, J. Eur. Ceram. Soc. 34 (2014) 4117–4130.
[3] G. Strauch Lindemann, Properties of direct aluminum bonded substrates for power semiconductor components, IEEE Trans. Power Electron. 22 (2007) 384–391.
[4] T.G. Lei, J.N. Calata, K.D.T. Ngo, G.Q. Lu, Effects of large-temperature cycling range on direct bond aluminum substrate, IEEE Trans. Device Mater. Reliab. 9 (2009) 563–568.
[5] G. Chen, K. Lin, C. Lin, Aging effect on high heat dissipation DBA and DBAC substrates for high power electronics, Ceram. Int. 48 (2022) 28889–28897.
[6] D. Kim, C. Chen, S. Nagao, et al., Mechanical characteristics and fracture behavior of GaN/DBA die-attached during thermal aging: pressure-less hybrid Ag sinter joint and Pb–5Sn solder joint, J. Mater. Sci. Mater. Electron. 31 (2020) 587–598.
[7] Z. Ran, H. Shang, B. Ma, R. Li, F. Shangguan, D. Yu, Microstructure and mechanical properties of AlN/Al joints brazing by a sputtering Al/Cu bilayer film solder, Materials 15 (7) (2022) 2674.
[8] Y. Wang, Y. Cheng, C. Lin, K. Lin, Direct bonding of aluminum to alumina using a nickel interlayer for power electronics applications, Results Mater 6 (2020) 100093.

[9] M. Fei, R. Fu, S. Agathopoulos, J. Fang, C. Wang, H. Zhu, A preparation method for Al/AlN ceramics substrates by using a CuO interlayer, Mater. Des. 130 (2017) 373–380.
[10] J. Wang, K. Chuang, Y.-C. Wu, M.-H. Ku, S.-W. Ku, M.-W. Wu, Mechanical performances of AlN/Al metallized ceramic substrates fabricated by transient liquid phase bonding and pre-oxidation treatment, Ceram. Int. 48 (2022) 16619–16629.
[11] C. Imediegwu, S. Graham, D.G. Pahinkar, S. Narumanchi, P. Paret, J. Major, Interdiffusion and formation of intermetallic compounds in high-temperature power electronics substrate joints fabricated by transient liquid phase bonding, Microelectron. Reliab. 137 (2022) 114788.
[12] C.H. Hsueh, A.G. Evans, Residual stresses in metal/ceramic bonded strips, J. Am. Ceram. Soc. 68 (2006) 241–248.
[13] C. Wallis, B. Buchmayr, R. Bermejo, P. Supancic, Fabrication of 3D metal-ceramic (Al-AlN) architectures using laser-powder bed fusion process, Addit. Manuf. 38 (2021) 101799.
[14] Kara-Slimane, D. Juve, E. Leblond, D. Treheux, Joining of AlN with metals and alloys, J. Eur. Ceram. Soc. 20 (2000) 1829–1836.
[15] K.S. Siow, Are sintered silver joints ready for use as interconnect material in microelectronic packaging? J. Electron. Mater. 43 (2014) 947–961.
[16] P. Peng, A. Hu, A.P. Gerlich, G. Zou, L. Liu, Y. Norman Zhou, Joining of silver nanomaterials at low temperatures: processes, properties, and applications, ACS Appl. Mater. Interfaces 7 (23) (2015) 12597–12618.
[17] S.A. Paknejad, S.H. Mannan, Review of silver nanoparticle based die attach materials for high power/temperature applications, Microelectron. Reliab. 70 (2017) 1–11.
[18] Z. Zhang, G.-Q. Lu, Pressure-assisted low-temperature sintering of silver paste as an alternative die-attach solution to solder reflow, IEEE Trans. Electron. Packag. Manuf. 25 (4) (2002) 279–283.
[19] K.S. Siow, Y.T. Lin, Identifying the development state of sintered silver (Ag) as a bonding material in the microelectronic packaging via a patent landscape study, J. Electron. Packag. 138 (2016) 020804.
[20] F. Yang, W. Zhu, W. Wu, H. Ji, C. Hang, M. Li, Microstructural evolution and degradation mechanism of SiC–Cu chip attachment using sintered nano-Ag paste during high-temperature ageing, J. Alloys Compd. 846 (2020) 156442.
[21] C. Chen, Z. Zhang, Q. Wang, B. Zhang, Y. Gao, T. Sasamura, Y. Oda, N. Ma, K. Suganuma, Robust bonding and thermal-stable Ag–Au joint on ENEPIG substrate by micron-scale sinter Ag joining in low temperature pressure-less, J. Alloys Compd. 828 (2020) 154397.
[22] Q. Xu, Y. Mei, X. Li, G.-Q. Lu, Correlation between interfacial microstructure and bonding strength of sintered nanosilver on ENIG and electroplated Ni/Au direct-bond-copper (DBC) substrates, J. Alloys Compd. 675 (2016) 317–324.
[23] J. Zähr, S. Oswald, M. Türpe, H.J. Ullrich, U. Füssel, Characterisation of oxide and hydroxide layers on technical aluminum materials using XPS, Vacuum 86 (2012) 1216–1219.
[24] R. Manikam, K.A. Razak, K.Y. Cheong, Sintering of silver–aluminum nanopaste with varying aluminum weight percent for use as a high-temperature die-attach material, IEEE Trans. Compon. Packag. Manuf. 2 (2012) 1940–1948.
[25] C. Chen, K. Suganuma, Large-scale ceramic–metal joining by nano-grained Ag particles paste sintering in low-temperature pressure-less conditions, Scripta Mater. 195 (2021) 113747.
[26] K. Motoyama, T. Matsuda, T. Sano, et al., AlN-to-metal direct bonding process utilizing sintering of Ag nanoparticles derived from the reduction of Ag2O, J. Electron. Mater. 47 (2018) 5780–5787.
[27] H. Zhang, W. Li, Y. Gao, et al., Enhancing low-temperature and pressureless sintering of micron silver paste based on an ether-type solvent, J. Electron. Mater. 46 (2017) 5201–5208.
[28] H. Zhang, C. Chen, J. Jiu, et al., High-temperature reliability of low-temperature and pressureless micron Ag sintered joints for die attachment in high-power devices, J. Mater. Sci. Mater. Electron. 29 (2018) 8854–8862.
[29] J. Jiu, H. Zhang, S. Nagao, et al., Die-attaching silver paste based on a novel solvent for high-power semiconductor devices, J. Mater. Sci. 51 (2016) 3422–3430.
[30] Y. Li, H. Wang, L. Weng, et al., Wetting and spreading of AgCuTi on Fe substrate at high temperatures: a molecular dynamics study, J. Mater. Res. Technol. 27 (2023) 5783–5790.
[31] C. Chen, J. Yeom, C. Choe, et al., Necking growth and mechanical properties of sintered Ag particles with different shapes under air and N_2 atmosphere, J. Mater. Sci. 54 (2019) 13344–13357.
[32] M. Mazlan, N. Jamadon, A. Rajabi, et al., Necking mechanism under various sintering process parameters – a review, J. Mater. Res. Technol. 23 (2023) 2189–2201.
[33] C. Chen, D. Kim, Z. Zhang, et al., Interface-mechanical and thermal characteristics of Ag sinter joining on bare DBA substrate during aging, thermal shock and 1200 W/cm^2 power cycling tests, IEEE Trans. Power Electron. 37 (2022) 6647–6659.
[34] C. Chen, Z. Zhang, D. Kim, et al., Interface reaction and evolution of micron-sized Ag particles paste joining on electroless Ni-/Pd-/Au-finished DBA and DBC substrates during extreme thermal shock test, J. Alloys Compd. 862 (2021) 158596.
[35] C. Du, G. Zou, J. Huo, et al., Generative AI-enabled microstructure design of porous thermal interface materials with desired effective thermal conductivity, J. Mater. Sci. 58 (2023) 16160–16171.
[36] K. Park, D. Seo, J. Lee, Conductivity of silver paste prepared from nanoparticles, Colloids Surf. A Physicochem. Eng. Asp. 313–314 (2008) 351–354.
[37] E. Jo, Y.R. Kim, S. Lee, et al., Oxidation-free silver porous sheet bonding onto a bare copper substrate in air, Mater. Lett. 378 (2024) 137633.
[38] D. Kim, M. Kim, Macroscale and microscale structural mechanisms capable of delaying the fracture of low-temperature and rapid pressureless Ag sintered electronics packaging, Mater. Char. 198 (2023) 112758.
[39] S. Wang, M. Li, H. Ji, et al., Rapid pressureless low-temperature sintering of Ag nanoparticles for high-power density electronic packaging, Scripta Mater. 69 (2013) 789–792.
[40] E. Ide, S. Angata, A. Hirose, et al., Metal–metal bonding process using Ag metallo-organic nanoparticles, Acta Mater. 53 (2005) 2385–2393.
[41] Y. Tao, G. Ke, Y. Xie, et al., Adhesion strength and nucleation thermodynamics of four metals (Al, Cu, Ti, Zr) on AlN substrates, Appl. Surf. Sci. 357 (2015) 8–13.
[42] S. Zhang, W. Jin, H. Yang, et al., Comparative study of Ti and Cr adhesion to the AlN ceramic: experiments and calculations, Appl. Surf. Sci. 457 (2018) 856–862.
[43] P. Rong, H. Zhou, X. Ning, et al., Bonding strength and mechanism between aluminum and AlN, J. Inorg. Mater. 26 (2011) 249–253.
[44] F. Huo, C. Chen, Z. Zhang, et al., Interface regulation of micro-sized sintered Ag-10Al composite based on in-situ surface modification and enhanced microstructure stability in power electronic packaging, Mater. Des. 240 (2024) 112863.
[45] C. Chen, A. Suetake, F. Huo, et al., Development of SiC power module structure by micron-sized Ag-paste sinter joining on both die and heatsink to low-thermal-resistance and superior power cycling reliability, IEEE Trans. Power Electron. 39 (2024) 10638–10650.
[46] Y.L. Müller, L.P.H. Jeurgens, A. Antušek, et al., Atomistic assessment of melting point depression and enhanced interfacial diffusion of Cu in confinement with AlN, ACS Appl. Mater. Interfaces 14 (2022) 26099–26115.
[47] M. Chiodi, C. Cancellieri, F. Moszner, et al., Massive Ag migration through metal/ceramic nano-multilayers: an interplay between temperature, stress-relaxation and oxygen-enhanced mass transport, J. Mater. Chem. C 4 (2016) 4927–4938.
[48] N. Matsuhisa, D. Inoue, P. Zalar, et al., Printable elastic conductors by in situ formation of silver nanoparticles from silver flakes, Nat. Mater. 16 (2017) 834–840.
[49] C. Chen, K. Suganuma, Microstructure and mechanical properties of sintered Ag particles with flake and spherical shape from nano to micro size, Mater. Des. 162 (2019) 311–321.
[50] B. Xiao, G. Wu, T. Wang, et al., Enhanced Li-ion diffusion and cycling stability of Ni-free high-entropy spinel oxide anodes with high-concentration oxygen vacancies, ACS Appl. Mater. Interfaces 15 (2023) 2792–2803.
[51] D.S. Banks, C. Fradin, Anomalous diffusion of proteins due to molecular crowding, Biophys. J. 89 (2005) 2960–2971.
[52] R. Meyer, Q. Ge, J. Lockemeyer, et al., An ab initio analysis of adsorption and diffusion of silver atoms on alumina surfaces, Surf. Sci. 601 (2007) 134–145.
[53] E.G. Gontier-Moya, J. Bernardini, F. Moya, Silver and platinum diffusion in alumina single crystals, Acta Mater. 49 (2001) 637–644.
[54] H. Oughaddou, S. Vizzini, B. Aufray, et al., Growth and oxidation of aluminum thin films deposited on Ag(111), Appl. Surf. Sci. 252 (2006) 4167–4170.